ADVANCED FUNCTIONAL MATERIALS
www.afm-journal.de

# A Self-Powered, Highly Sensitive, and Frequency-Tunable Triboelectric Acoustic Sensor Inspired by the Human Cochlea

*Dong-hee Kang, Hyejin Lee, Minseop Song, Yun Goo Ro, Min Sub Kwak, Jinyoung Kim, Geonyoung Jung, Jonghwa Park, Young-Ryul Kim, Jiin Lee, Jae Joon Kim,* and Hyunhyub Ko**

**Conventional acoustic sensors used in human–machine interfaces often face challenges such as power supply requirements, limited sensitivity, and inability to tune their frequency response. A self-powered, highly sensitive, and frequency-tunable triboelectric acoustic sensor inspired by the human cochlea is introduced. By mimicking hair cells in the organ of Corti, a tapered microhair-structured ferroelectric poly(vinylidene fluoride-co-hexafluoropropylene) (PVDF-HFP) and barium titanate nanoparticle (BTNP) composite film is proposed, which demonstrates a 16-fold increase in triboelectric output voltage (1.3 V) compared to a planar one at 2.8 Pa. Furthermore, inspired by the frequency selectivity of the basilar membrane with gradient structural variations, integrating a mass-beam diaphragm is proposed with varying kirigami length and circular mass diameter that enables precise tuning of the resonance frequency of the sensor, resulting in a 32 times improvement in sensitivity (860 mV $Pa^{-1}$) compared to a nonbiomimetic sensor (28 mV $Pa^{-1}$) and an expanded dynamic range. The proposed sensor differentiates between human voices with different frequencies. A robotic hand integrated with the sensor responds to acoustic stimuli with programmed hand gestures, which highlights its potential in acoustic human–machine interfaces. The biomimetic approach to developing a self-powered, highly sensitive, and frequency-tunable acoustic sensor offers new possibilities for intuitive and immersive human–machine interfaces.**

## 1. Introduction

There is a growing trend toward the utilization of acoustic devices as pivotal interfaces facilitating the connection between humans and machines. Representative applications for acoustic human–machine interfaces encompass various fields, including virtual reality (VR) and augmented reality (AR) devices, robotics, smart home devices, and automotive interfaces.[1–4] In these fields, the incorporation of acoustic devices has revolutionized the way users interact with machines, offering enhanced immersion, functionality, and convenience. For instance, in VR and AR devices, acoustic interfaces enable users to experience immersive audio environments, adding depth and realism to virtual experiences.[5,6] In robotics, these interfaces empower machines to perceive and respond to auditory cues, facilitating more intuitive human–robot interaction and enhancing collaborative capabilities.[7–10] Central to the effectiveness of these interfaces is the seamless integration of acoustic devices, which necessitates the development of lightweight, self-powered systems capable of accurate voice recognition. However, conventional acoustic devices designed for human–machine interfaces suffer from several limitations, including the necessity for a constant power source,[11,12] low sensitivity to acoustic stimuli,[13] and the inability to selectively process signals.[14]

To address these challenges, extensive research has been conducted by introducing composite materials[15–17] and structural modification,[18–20] employing various mechanisms, including piezoresistive,[15–18] capacitive,[12,21,22] electromagnetic,[23–25] piezoelectric,[6,26–33] and triboelectric[8,19,20,34] methods. Piezoresistive acoustic sensors offer benefits such as noise insensitivity, easy integration, and direct signal translation.[16,18] However, they require an external power supply, nonflat frequency response, narrow frequency bandwidth, and nonlinear output signals. Capacitive sensors are known for their linear output signals, durability, and stable sensitivity across a broad frequency range[21,22] but are hindered by low output signals in the presence

D.-hee Kang, H. Lee, Y. G. Ro, M. S. Kwak, J. Kim, G. Jung, J. Park, Y.-R. Kim, J. Lee, H. Ko
School of Energy and Chemical Engineering
Ulsan National Institute of Science and Technology (UNIST)
Ulsan 44919, Republic of Korea
E-mail: hyunhko@unist.ac.kr
M. Song, J. J. Kim
Department of Electrical Engineering
Ulsan National Institute of Science and Technology (UNIST)
Ulsan 44919, Republic of Korea
E-mail: jaejoon@unist.ac.kr
The ORCID identification number(s) for the author(s) of this article can be found under https://doi.org/10.1002/adfm.202408344



**DOI: 10.1002/adfm.202408344**

of surrounding noise and the requirement for a constant voltage source. For piezoresistive and capacitive sensors, the power supply issue is still a main concern. In contrast, electromagnetic, piezoelectric, and triboelectric sensors present a significant advantage in acoustic devices due to their self-powered operation. This capability is particularly beneficial in overcoming the limitations posed by bulky energy sources, which often restrict the form factor of these devices. Despite these benefits, electromagnetic sensors may suffer from surrounding electromagnetic interference and low sensitivity.[35] Piezoelectric sensors may experience electric charge leakage and may need an external power source to amplify the small amount of output signals.[26] Triboelectric sensors are bound by the device's inherent resonance frequency due to their larger sensor dimension compared to other mechanisms.[36]

While triboelectric sensors offer the advantages of self-powering, they may face challenges in achieving frequency selectivity in a single device. Previous research concerning acoustic devices that achieve frequency selectivity has involved the complex process of fabricating array-type devices by modifying the device's dimensions.[8,34,37] In addition, there is an optimal size for triboelectric devices to maximize contact separation.[38,39] Altering the dimensions of a device can lead to variations in the displacement of its layers, making it crucial to achieve frequency tuning at an optimal device dimension. Frequency selectivity is essential in acoustic devices as it allows for the differentiation and isolation of specific frequencies or ranges of frequencies from ambient noise.[8,37,40] In applications such as speech recognition or acoustic human–machine interfaces, where accurate detection and analysis of specific frequency components are essential, frequency selectivity plays a pivotal role in ensuring the device's efficacy and reliability. The ability to achieve frequency selectivity is not only desirable but also indispensable for advancing the functionality and performance of acoustic devices.

To address the limitations of conventional triboelectric acoustic sensors, we propose a system designed to fine-tune the frequency response by modifying the diaphragm dimensions of biomimetically inspired triboelectric acoustic sensors. By emulating the architecture of the cochlea's hair cells, we have developed an acoustic sensor that exhibits exquisite sensitivity to auditory stimuli. Recent studies have highlighted the effective use of micropillars in a sensitive pressure-sensing matrix, which benefits from pressure-induced deformation and charge separation.[17,41,42] In our study, we utilize poly(vinylidene fluoride-co-hexafluoropropylene) (PVDF-HFP), a ferroelectric polymer, to create a unique structure known as a "microhair"—a tapered micropillar with an extended aspect ratio. This innovative design significantly enhances the negative charge generation on the microhair's surfaces as well as the pressure-induced deformation, owing to the inherent material properties of PVDF-HFP and the structural benefits of the tapered microhair design. To circumvent the fixed resonance frequency limitation associated with the conventional triboelectric acoustic sensors, we have engineered a microscale patterned diaphragm that can tune the resonance frequency range of the acoustic sensor. Inspired by the structural differences in the cochlea's basilar membrane, this diaphragm features a distinctive structure comprising a central circle of mass connected to three kirigami-patterned beams. Adjusting the resonance frequency of our acoustic sensor is accomplished by manipulating two aspects of the diaphragm: the radius of the central circle[43] and the length of kirigami cut patterns.[44] Altering the diameter of the circular mass changes the void space of the diaphragm, thereby enabling tunable resonance frequency of the sensors. Tuning the resonance frequency of the fabricated sensor can offer a convenient acoustic platform for customized human–machine interfaces.

## 2. Results and Discussion

### 2.1. Frequency Tunable Acoustic Sensor inspired by the Human Cochlea

Acoustic signals from the external environment enter the human ear as waves and are converted into mechanical vibrations by the tympanic membrane, or eardrum, in the outer ear. These vibrations travel through the middle ear and reach the cochlea in the inner ear, where a fluid called the lymph transmits the vibrations. **Figure 1a** illustrates the cochlea, which houses specialized regions for detecting different sound frequencies. Within the cochlea lies the organ of Corti, which comprises three primary elements: the basilar membrane, outer/inner hair cells, and tectorial membrane (Figure 1b; Figure S1a, Supporting information). As the cochlear fluid vibrates, it stimulates the basilar membrane, which varies in thickness, modulus, and width, allowing it to resonate at specific frequencies. The outer hair cells play a crucial role in amplifying these vibrations, enhancing the sensitivity and frequency selectivity of the cochlea. This amplified mechanical motion then causes the inner hair cells to deflect, opening ion channels and converting mechanical energy into neural signals, which are then transmitted to the brain (Figure S1b, Supporting information).[45,46] To emulate the complex structure of the organ of Corti, we have engineered a microhair pattern that functions as both a signal-amplifying and signal-sensing layer, a Kapton diaphragm as a frequency tuning layer, and substrates with a circular aperture for covering the thin parylene film (Figure 1c). The fabrication of microhair pattern and Kapton diaphragm mimics the sound sensing system and the frequency selectivity of the human cochlea. The kinetic energy carried by sound frequencies, in the form of dynamic pressure from acoustic stimuli, induces contact separation in both the microhair pattern and a thin aluminum electrode film. This interaction generates a triboelectric effect, transforming acoustic energy into electrical signals (Figure 1d).

In the human cochlea, the mechanical properties of the basilar membrane differ along its length, facilitating the detection of a range of resonance frequencies in different regions. This variation is due to the increasing width and thickness of the basilar membrane as it extends deeper into the cochlea, resulting in a lower resonance frequency.[46,47] Emulating this gradation, we have created graded diaphragm structures by using laser-ablated Kapton films with a central mass connected by three beams (Figure 1e). By adjusting the diameter of the circular mass, we can tune the sensitivity of our sensor to the specific resonance frequency of the Kapton diaphragm, which decreases as the mass diameter increases. The self-powered operation of the acoustic sensor is detailed in Figure S2 (Supporting information). The working mechanism of our sensor is based on the triboelectric mechanism, which enables the sensing of mechanical stimuli

 

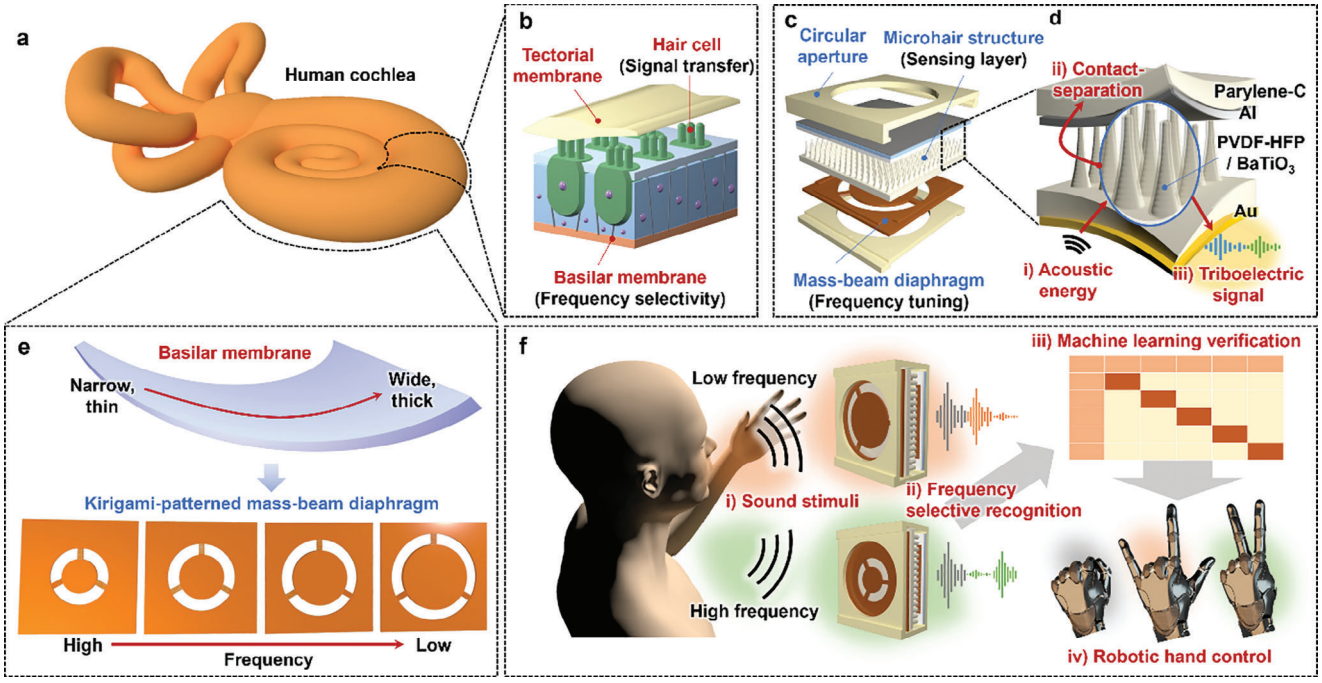


**Figure 1.** Triboelectric acoustic sensor mimicking the cochlea's hair cells. a) Schematic of the human cochlea. b) Organ of Corti inside the human cochlea. c) Fabricated tapered microhair sensor with a Kapton diaphragm. d) Sensing matrix of the fabricated tapered microhair sensor. Applied acoustic energy induces contact separation between the microhair structure and Al-coated Parylene-C film, resulting in a triboelectric signal. e) Schematic of the human basilar membrane and the fabricated mass-beam structured Kapton diaphragm. f) Schematics of the applications as an acoustic human–machine interface for the designed frequency tuning system.

through the interaction of two differently charged layers undergoing a contact-separation process. This triboelectric mechanism allows for self-powered sensing of mechanical stimuli by generating electrical signals from the charge difference between the two layers. When sound waves impinge upon the sensor, they induce contact separation between the microhair medium and the thin Parylene-C film. This contact-separation movement generates triboelectric signals due to the potential difference between the PVDF-HFP and aluminum layers. The few tens of micrometer-sized microhair structures likely experience a complex deformation pattern. Given the tapered shape of the microhairs, we hypothesize that they undergo a combination of lateral bending, particularly at the tips, and some degree of vertical compression. This combined movement could enhance the contact-separation process between the two different films, potentially increasing the effective contact area during acoustic stimulation. However, we acknowledge that the exact nature of this deformation requires further investigation through detailed simulations and high-resolution imaging studies. Such research could provide valuable insights for optimizing sensitivity and efficiency of our sensor. Importantly, this mechanism directly produces the output signal of the sensor without requiring an external power source, making it truly self-powered. The inclusion of a Kapton diaphragm beneath the microhair structure allows the Kapton to vibrate at its own resonance frequency, transferring these vibrational responses at specific resonance frequencies to the microhair layer, which in turn resonates at different frequencies. By tuning the resonance frequency region of the fabricated sensor, selective sound recognition can be achieved with a single sensor device. To verify the frequency tuning system, we demonstrated a machine-learning process and confirmed that the frequency tuning system could be applied to the acoustic human–machine interfaces by controlling a robotic hand (Figure 1f).

The pressure response of the sensor was significantly enhanced by incorporating a ferroelectric polymer, PVDF-HFP, blended with piezoelectric ceramic barium titanate nanoparticles (BTNPs). The use of a ferroelectric PVDF-HFP/BTNP composite allows for the exploitation of the material's intrinsic ferroelectric polarization during the triboelectrification process. When subjected to mechanical stress, these materials undergo stress-induced polarization, which contributes to charge redistribution and increases the surface charge density on the triboelectric layer. The high dielectric constant of BTNP further amplifies this effect by enhancing the overall capacitance of the composite. Additionally, the stress concentration at the interfaces between PVDF-HFP and BTNP intensifies the piezoelectric response, resulting in a synergistic enhancement of the triboelectric output.[8,48] To further elucidate the mechanism of our self-powered acoustic sensor, we conducted comparative measurements of the output current during the contact-separation process between an Al film and a PVDF-HFP/BTNP film, as well as between two identical PVDF-HFP/BTNP films (Figure S3, Supporting information). The results show that the output current from the Al film and PVDF-HFP/BTNP film combination is ten times higher than that of two identical PVDF-HFP/BTNP films. This result confirms that the triboelectric effect is the major working mechanism of our sensor, assisted by a minor piezoelectric effect. Among various ferroelectric polymers, PVDF-HFP was chosen

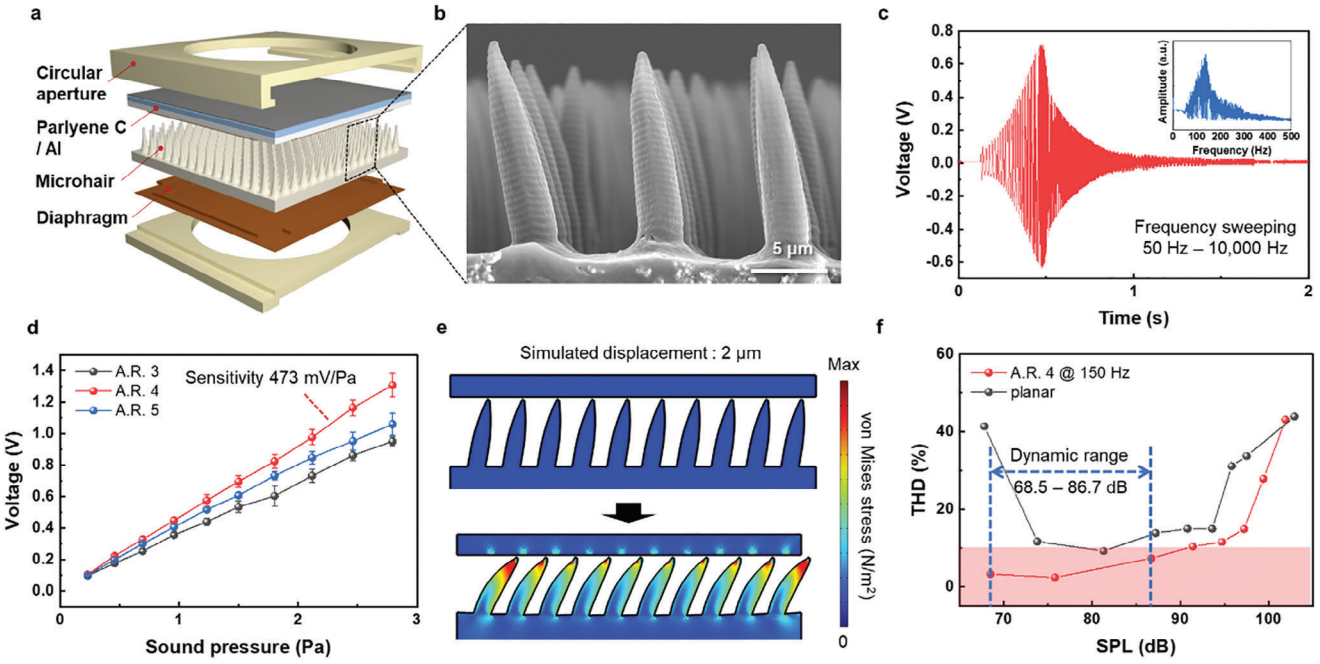


**Figure 2.** Acoustic performances of triboelectric sensors with different tapered microhair structures. a) Schematic of the fabricated tapered microhair sensor with a planar diaphragm. b) SEM image of the fabricated tapered microhair pattern made of PVDF-HFP/BTNP composite (scale bar = 5 μm). c) Voltage output at frequencies swept from 50 to 10 000 Hz. Inset: Fast-Fourier transform (FFT) data of the voltage output, showing a resonance frequency peak ≈150 Hz. d) Plot of voltage output with changing applied sound pressure levels at 150 Hz. The tapered microhair with an aspect ratio of 4 showed the highest sensitivity. e) Simulation of von Mises stress at a 2-micrometer displacement. f) Comparison of total harmonic distortion (THD) between the fabricated acoustic sensor with the tapered microhair structure and a planar film.

for its relatively low modulus (4.7 ± 0.5 MPa) compared to other fluorine-based ferroelectric materials.[49,50] In addition, the incorporation of BTNP not only enhances the ferroelectric properties of the composite but also concentrates the applied stress due to the inherent rigidity of BTNPs.[8,51] There's an optimum point of the concentration of BTNPs in the composite film, showing the best dielectric performance before dielectric breakdown.[52] As shown in Figure S4 (Supporting information), films with 7 wt.% BTNP exhibited the highest relative permittivity ($\epsilon_r$), indicating enhanced electrical charge storage capabilities. Likewise, PVDF-HFP with 7 wt.% BTNP shows the highest polarization (Figure S5, Supporting information). Although polarization increases with BTNP contents, PVDF-HFP with 10 wt.% BTNP has lower polarization than that with 7 wt.% BTNP because a large amount of BTNP forms an electrical leakage path and induces dielectric loss.

### 2.2. Acoustic Performances of Triboelectric Acoustic Sensors with Different Microhair Structures

**Figure** 2a illustrates the constructed triboelectric acoustic sensor, consisting of an upper aluminum layer and a lower PVDF-HFP/BTNP composite layer formed into microhair arrays, enveloped by a Kapton diaphragm, and supported by top and bottom substrates with a circular aperture. This configuration ensures the sensor's accurate response to specific sound frequencies by stabilizing both the sensor and diaphragm. This design is inspired by the human hair cell within the organ of Corti, characterized by a vertically standing, hair-like structure that responds sensitively in response to vibrational signals in the cochlea. The tapered design of the microhairs in our sensor is a deliberate emulation of these human hair cells, aimed at enhancing sensitivity to acoustic stimuli. For the fabrication of PVDF-HFP/BTNP microhairs, we first fabricated silicon microhair structures, as detailed in Figures S6 and S7 (Supporting information), with the resulting structures and their various aspect ratios shown as SEM images in Figure S8 (Supporting information). Then, we replicated the silicon microhair structures by using a replica molding process. Given the high aspect ratio of silicon microhairs, a self-assembly monolayer (SAM) of fluoro-octyltrichloro-silane (FOTS) was applied, followed by micro-molding in poly(dimethylsiloxane) (PDMS), as illustrated in Figure S9a (Supporting information). This SAM coating process is essential to facilitate the release of the PDMS mold from the silicon microhairs. The composite solution was then molded over this pattern to form the PVDF-HFP/BTNP microhairs (Figure S9b, Supporting information). Figure 2b and Figure S10 (Supporting information) display SEM images of these patterns with differing aspect ratios.

The output voltage response of our sensor is illustrated in Figure 2c showing peak-to-peak voltage ($V_{pp}$) of 1.3 V at its resonance frequency, during a frequency sweeping test covering a range from 50 to 10 000 Hz. Figure S11 (Supporting information) shows the STFT data of the frequency sweeping test in Figure 2c. The colors in the STFT graph represent the intensity of the frequency signal over time, which indicates the wideband working frequency range from 50 to 10 000 Hz. The fabricated

microhair structure exhibited an inherent resonance peak ≈150 Hz, as shown in the inset of Figure 2c. The setup for the detailed measurement is depicted in Figure S12 (Supporting information). A commercial speaker connected to a frequency oscillator was employed to generate sound, with the sensor's output voltage data captured by an oscilloscope. The ambient noise in the anechoic chamber was ≈20 mV (Figure S13, Supporting information). Figure 2d presents the voltage output of sensors with varying aspect ratios at different sound pressures, all at the same sound frequency of 150 Hz. It was observed that the sensor structure with an aspect ratio of 4 demonstrated the highest voltage output.

Further insights into the effect of microhair structure and its aspect ratio on the sensor performance are provided by simulations of von Mises stress depending on the deformation and triboelectric potential difference (Figure S14, Supporting information). By introducing microstructure on the film surface, the stress levels and electrification between two different layers increase dramatically.[53–55] Hence, the sensor with microstructures can sense minute pressure such as acoustic signals very sensitively. Interestingly, stress levels increase as aspect ratios decrease even though larger aspect ratios result in a greater triboelectric potential difference, suggesting the existence of an optimal aspect ratio for maximized voltage output and sensitivity. Detailed information about the simulation setup is available in Note S1 (Supporting information). The optimal point is determined to be an aspect ratio of 4, as evidenced by the highest voltage output of 1.3 V at 2.8 Pa and a sensitivity of 473 mV $Pa^{-1}$ (measured as the slope of the graph in mV $Pa^{-1}$) in Figure 2d. The impact of the microhair structure on the sensor performance was further investigated by fabricating nontapered microhairs with varying aspect ratios using the same composite material (Figure S15, Supporting information). The results in Figure S16 (Supporting information) show that the peak voltage output for these nontapered structures also occurred at an aspect ratio of 4. Tapered microhair structures exhibited a higher output voltage of 1.3 V at an applied sound pressure of 2.8 Pa, which is more than twice the value compared to nontapered structures, 0.7 V. When compared to the planar structure (0.081 V), the tapered microhair structure showed a 16 times higher output voltage at the sound pressure of 2.8 Pa. For quantitative comparison of sensitivity among different patterns, we have calculated the sensitivity of 3 different patterns. The sensitivity is calculated by calculating the slope of the graph. Tapered microhair with an aspect ratio of 4 showed 473 mV $Pa^{-1}$, nontapered structure with an aspect ratio of 4 showed 237, and 28 mV $Pa^{-1}$ for planar structure, which has no pattern. This result exhibits the superior sensitivity of the tapered microhair structure to acoustic stimuli, highlighting the effectiveness of our biomimetic design approach.

In Figure 2e, the simulated von Mises stress for the microhairs before and after a displacement of 2 μm is displayed. The tapered structure, compared to its nontapered counterpart, exhibits significantly higher maximum stress (Figure S17, Supporting information). In addition, we calculated the total harmonic distortion (THD), which indicates the distortion level of the original sound. The lower the THD, the more accurate the sound response within the sensing matrix. The performance of the microphone can be quantified by the THD value, calculated using the following formula.

$$THD\ (\%) = \frac{\sqrt{A_2{}^2 + A_3{}^2 + A_4{}^2 + A_5{}^2 + \cdots}}{A_1} \times 100 \quad (1)$$

In this equation, $A_x$ represents the amplitude at the $x^{th}$ harmonic frequency. By applying the fast Fourier transform (FFT) to the voltage readings at specific frequencies, we obtain amplitude values for the harmonic frequencies. The THD value is then derived by dividing the sum of these harmonics by the original amplitude. Microphones with a THD of less than 10% are generally considered to be high-performing, characterized by their clear sound reproduction capabilities.[2] Moreover, the sound pressure level (SPL) range within which the THD remains below 10% defines the dynamic range of the acoustic sensor. This range indicates the SPL levels that the acoustic sensor can accurately capture without significant distortion. As shown in Figure 2f, the calculated dynamic range for the microhair acoustic sensor spans from 68.5 to 86.7 dB for a 150 Hz sound stimulus. Compared to the planar PVDF-HFP/BTNP film, the acoustic sensor fabricated with the microhair structured film showed a lower THD value due to the enhanced charge potential and surface polarization. This result indicates that the microhair sensor operates accurately within the mentioned sound pressure level range. Compared to the capacitive acoustic sensor, showing a dynamic range of 50–80 dB,[21] our triboelectric sensor exhibits limitations in detecting lower sound pressure levels but shows advantages at higher levels.

### 2.3. Acoustic Performances of Triboelectric Acoustic Sensors with Different Diaphragm Structures

To enhance the response to the acoustic stimuli of the microhair structure, we employed laser ablation on Kapton films to create a mass suspended by three different beams. Drawing inspiration from structures such as the tri-leaf formation[43] and the use of an additional annular membrane for frequency-tunable acoustic devices,[19] the diaphragm's architecture can be finely adjusted to control the resonance frequency using a single film. The incorporation of a kirigami pattern within the mass-beam structure introduces variations in the rigidity of the suspended mass, thereby increasing the structure's responsiveness to vibratory stimuli.[56–59] **Figure 3a** presents schematics of the various diaphragm designs, including planar, mass-beam, and kirigami-patterned mass-beam structures. As the design evolves from a planar diaphragm to a kirigami-patterned mass-beam configuration, there is a noticeable increase in sensitivity by a factor of 1.8, from 473 to 860 mV $Pa^{-1}$, as evidenced in Figure 3b. The sensitivity (860 mV $Pa^{-1}$) of the triboelectric sensor with the tapered microhair and the kirigami-patterned mass-beam structures is 31 times higher than that (28 mV $Pa^{-1}$) of the sensor without these biomimetic structures. This refined approach to sensor and diaphragm structures marks a significant advancement in the precision and reliability of acoustic sensors, making them suitable for high-fidelity sound detection and analysis.

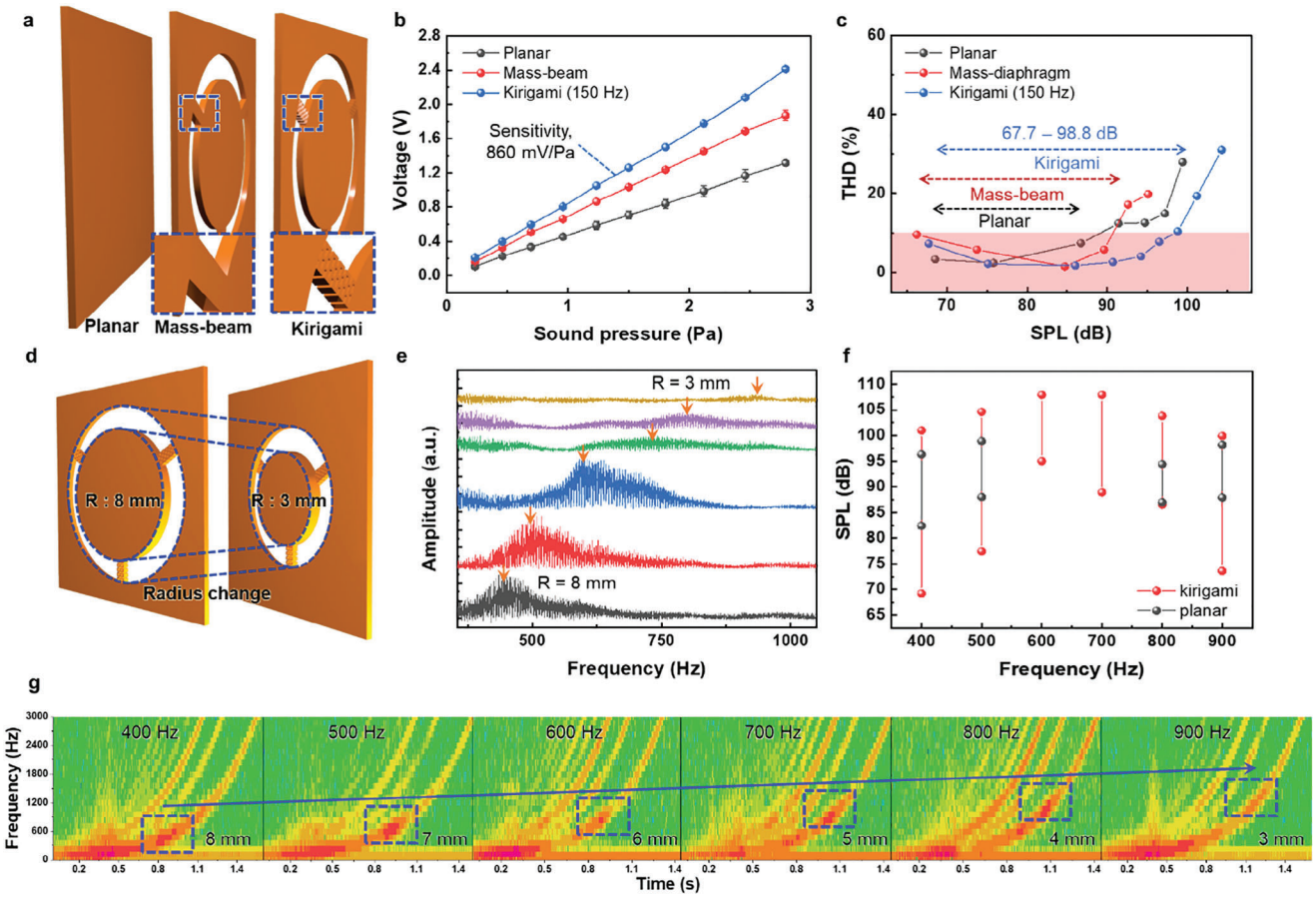


**Figure 3.** Acoustic performances of triboelectric sensors with different diaphragm structures. a) Schematic of the Kapton diaphragm introducing a mass-beam structure and a kirigami structure. b) Plot of the output voltage as a function of changing sound pressure at 150 Hz. The Kapton diaphragm with the kirigami structure shows the highest sensitivity of 860 mV $Pa^{-1}$. c) Total harmonic distortion (THD) of the fabricated sensor with different diaphragms. d) Schematics of the frequency tuning system using the Kapton diaphragm by changing the radius of the mass-beam structure. e) Fast-Fourier transform results of the sensors after the frequency sweeping test on the Kapton diaphragms with different radius. f) Dynamic range at the resonance frequency of each kirigami-structured mass-beam Kapton diaphragm with different radius compared to the planar diaphragm. g) Short-time Fourier transform (STFT) of the fabricated sensor with tuning of the resonance frequency. The resonance frequency of each Kapton diaphragm with different radius (R = 8 mm to R = 3 mm) is indicated by higher intensities (red).

Utilizing the voltage output data from Figure 3b, we can calculate the signal-to-noise ratio (SNR) using the formula below, thereby quantifying the sensor's performance.

$$SNR_{dB} = 10 \times \log_{10}\left(\frac{V_{signal}}{V_{noise}}\right)^2 \quad (2)$$

As shown in Equation (2), the SNR is expressed as the ratio of the signal power to the background noise power, often on a logarithmic decibel scale for practical comparison of acoustic signals. From the data in Figure 3b, the maximum voltage output was 2.4 V in response to a sound pressure of 2.8 Pa, with ambient noise at 7 mV, yielding a calculated SNR of 41.6 dB. This SNR value is higher than that reported for previous triboelectric devices,[8] but lower than for external power-supplied resistive sensors.[16] A detailed comparison of our acoustic device with those in previous reports is presented in Table S1 (Supporting Information). Moreover, the incorporation of a kirigami-patterned mass beam into the diaphragm has demonstrated a reduction in THD across a wider range of SPLs. As depicted in Figure 3c, the dynamic range of the sensor expanded from 68.5 to 86.7 dB in a planar diaphragm structure to 67.7–98.8 dB with the kirigami-patterned mass-beam structure. To verify the acoustic sensing frequency lower limit of the sensor, we measured THD values at acoustic frequencies below 100 Hz (50, 70, and 100 Hz), as shown in Figure S18 (Supporting information). The results demonstrate a reasonable dynamic range at each of these frequencies, confirming the ability of our sensor to operate effectively below 100 Hz. In addition, the performance of microhair acoustic sensor was evaluated by increasing the distance between the incident speaker and the fabricated sensor. Compared to planar and mass-beam structured diaphragms, the kirigami-patterned mass-beam structure showed excellent performance in increasing the distance. When positioned 5 cm away from the speaker, the voltage output of the sensor reached 120 mV (Figure S19, Supporting information), confirming the high sensitivity of the microhair sensor to minute acoustic signals.

In the human cochlea, frequency recognition capabilities are primarily determined by the basilar membrane located beneath the hair cells within the organ of Corti.[46] Variations in the width and stiffness of the basilar membrane result in changes in its resonance frequency, thereby enabling neural signal generation across a spectrum of frequencies. To mimic this biological mechanism, we adjusted the radius of the mass-beam structure and the length of kirigami ablation in our sensor design, effectively tuning the resonance frequency of the diaphragm film (Figure 3d). Further structural details of the diaphragm are illustrated in Figure S20 (Supporting information). Adjusting these parameters allows the diaphragm to oscillate at different frequencies, becoming stiffer and vibrating at higher frequencies with reduced radius and ablation length, and at lower frequencies when they are increased. Our sensor demonstrates wideband frequency sensing capabilities (Figure S11, Supporting information), similar to the cochlea. The key innovation lies in our frequency tuning system, similar to the frequency selectivity function of the basilar membrane. Adjusting the diaphragm parameters allows it to oscillate at different frequencies, becoming stiffer and vibrating at higher frequencies with reduced radius and ablation length, and at lower frequencies when these dimensions are increased. This tuning system acts as a spatial filter, allowing us to selectively amplify specific signals within the wideband frequency stimuli. By combining broad-spectrum sensitivity with targeted frequency amplification, our sensor achieves a balance between the wide frequency response of the cochlea and the specific frequency tuning necessary for practical applications. This feature enables user-selective responses in acoustic HMI systems, making it particularly advantageous for applications such as personalized voice assistant systems and other user-selective devices.[7–9,19]

Simulations on the kirigami-patterned mass-beam Kapton film (Figure S21, Supporting information) show that as the radius of the mass-beam structure decreases to 4 mm, the resonance frequency of the Kapton film increases to 1366.5 Hz. This demonstrates how adjusting the dimensional features of the Kapton film allows us to target specific resonance frequency regions, enabling more precise acoustic sensing and potential noise reduction in specific frequency ranges. The simulation is calculated based on the dimensional features of the Kapton film. Detailed information about the resonance frequency of Kapton film is provided in Note S2 (Supporting Information). Figure 3e presents amplitude values obtained from FFT data following frequency sweeps from 50 to 10 000 Hz. The magnified graph image is shown in Figure S22a,b (Supporting information). To clarify the sensor signal, we plotted the output voltage of our sensor over time (Figure S22c, Supporting information). These figures illustrate the emergence of an additional resonance frequency peak, apart from the sensor's inherent resonance at ≈150 Hz, as the radius is reduced from 8 to 3 mm, validating the effectiveness of frequency tuning across the 400–900 Hz range.

The acoustic performance at the diaphragm's resonance frequency was further evaluated by calculating the THD for each film (Figure S23, Supporting information). Compared to the planar diaphragm, the laser-ablated, kirigami-patterned mass-beam diaphragm exhibited a wider dynamic range at its resonance frequencies (Figure 3f). In Figure 3g, frequency sweeping tests were conducted to examine the effect of the diaphragm structure on the resonance frequency. Acoustic frequencies ranging from 50 to 10 000 Hz were applied to the sensors with different diaphragm structures. The short-time Fourier transform (STFT) was conducted based on the voltage output data from the frequency sweeping tests. The STFT analysis on the frequency sweep data for different diaphragms reveals intensity variations corresponding to the resonance frequency of each diaphragm structure. As the sweeping frequency of sound stimuli is applied, the response of the fabricated micro hair sensor is recorded as color variation in the STFT graphs, which are expressed in a color map that varies from red to green. Red regions in the STFT graph indicate areas of high intensity. In one sensor, there are two distinct red regions: the inherent resonance frequency at 150 Hz and the tuned frequency region by the kirigami-patterned mass-beam diaphragm, marked by a red dotted box. This box shifts to a higher frequency region, indicating the tuning effect. The experimental results demonstrate that as the radius within the mass-beam structure decreases, the corresponding resonance frequency of the diaphragm increases, which is consistent with the simulation results in Figure S21b (Supporting information). In the STFT graph, the line at the lowest position in the graph represents the sweeping output result, while the other lines represent the harmonic output results, which clarifies the analysis of resonance frequencies and their harmonic effects in the sensor's response. To verify the stability of our acoustic sensor, the output voltage was measured for 1000 s (Figure S24, Supporting information). The output voltage was well maintained throughout this period without noticeable degradation.

### 2.4. Frequency Tunability of Triboelectric Acoustic Sensors with Different Diaphragm Radius

Our sensor can differentiate between human voices with different frequencies. **Figure** 4a shows the schematics of applying male and female voices to the triboelectric acoustic sensor. Figure 4b shows the STFT results, visualizing distinct patterns for a male and female voice saying "Frequency tunable triboelectric sensor". In particular, it is worth noting that the sensor's diaphragm size plays a critical role in determining its frequency response characteristics. Specifically, a smaller diaphragm radius leads to a sensitivity peak at higher frequencies, whereas a larger diaphragm radius results in a peak sensitivity at lower frequencies. In Figure 4b, the sensor with a 4 mm radius diaphragm showed an enhanced response at higher frequencies, particularly ≈800–1000 Hz. Conversely, the sensor with an 8 mm radius diaphragm exhibited an enhanced response at lower frequencies, ≈300–600 Hz. This tunability enables the sensor to be customized for specific applications requiring sensitivity to particular frequency ranges, thereby demonstrating its versatility in detecting and distinguishing sounds with varying frequency components.

To verify the reliability of our sensor, diaphragms with different radii were fabricated and attached to the microhair sensors. Figure 4c shows the methodology for performing a machine learning analysis. Diaphragms with four different radii were utilized to explore the frequency tunability of the sensors. For the qualitative comparison of the resonance frequencies of the sensors, we employed an artificial neural network (ANN) model. The

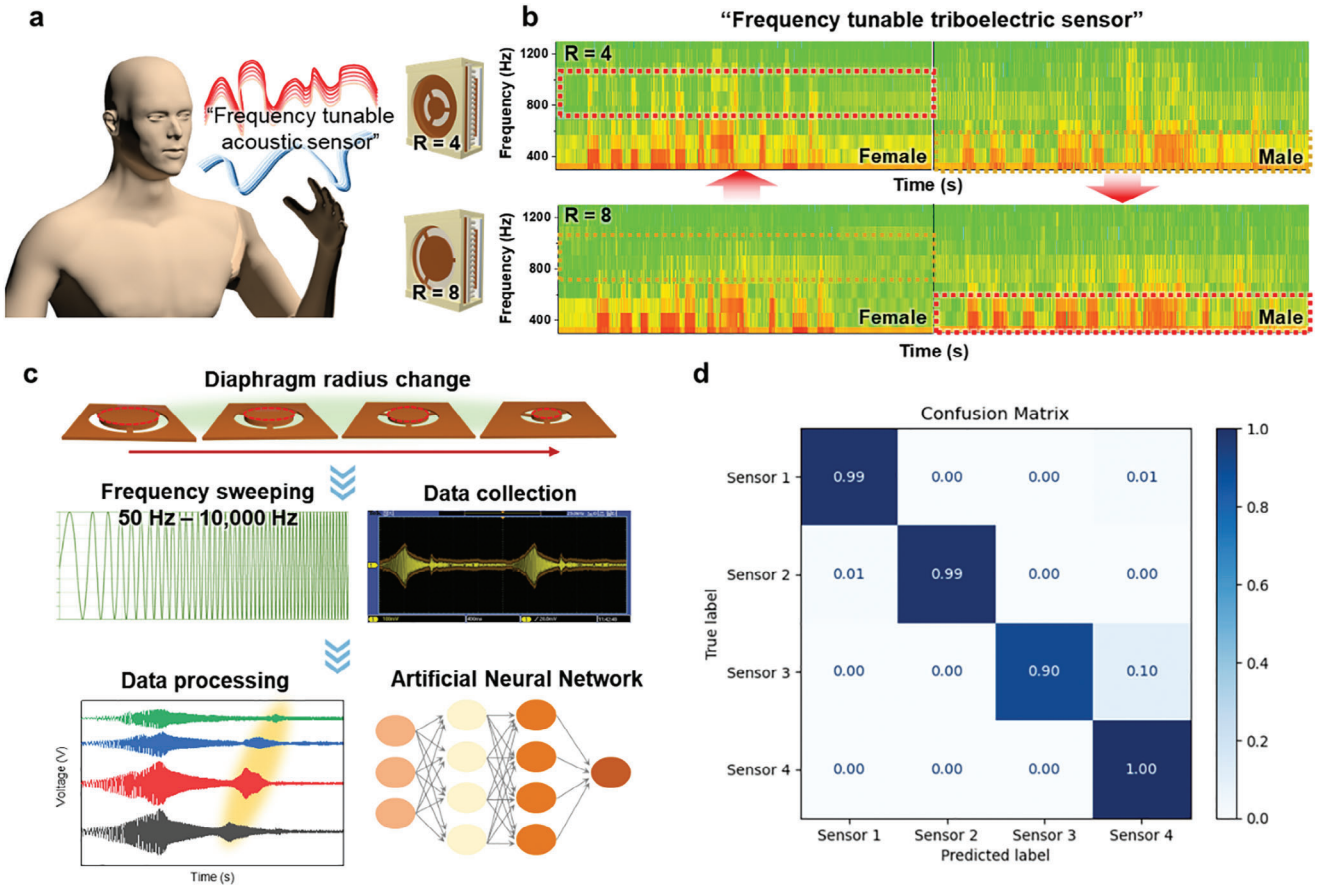


**Figure 4.** Frequency tunability of the triboelectric sensor with different diaphragm radius. a) Schematic of female and male voices applied to the fabricated sensors with Kapton diaphragms having different radius. b) Short-time Fourier transform (STFT) data of fabricated sensors having different diaphragm radius (R = 4 mm and R = 8 mm) after applying male and female voice profiles. The red dotted boxes indicate the signal enhancement in the tuned resonance frequency regions. c) Flow chart of the machine learning process for verifying the sensor's reliability in frequency tunability. d) Confusion matrix result of the frequency tuning system for 4 different Kapton diaphragm configurations.

ANN model is able to decipher complex and nonlinear patterns inherent in frequency-tuning data. The ANN model can qualitatively analyze the data by learning the relationships among nonlinear patterns and data from sensors in various situations, including images, acoustic sensing, and signal processing. This approach enables the evaluation of the varied frequency tuning system of our sensor, facilitating a comprehensive understanding of its diverse frequency components. Further details about the ANN model are provided in Note S3 (Supporting Information).

Our sensors exhibit a resonance frequency ≈150 Hz, stemming from the dimensional characteristics of sensors, and respond to different frequencies by tuning the frequency of the sensors. For sensor evaluation, the voltage response to sweeping acoustic stimuli frequencies was recorded. The acquired data were swept across a frequency range of 50–10 000 Hz. The applied sound stimuli were generated by a commercial speaker connected to a frequency oscillator. A voltage of 1 $V_{rms}$ was applied to the speaker, and the response of the microhair sensor was recorded using an oscilloscope. The data collected for verification were subjected to data slicing pre-processing for machine learning and labeled according to the sensors with different diaphragm radii. Figure 4d presents a confusion matrix, an essential tool for performance measurement in machine-learning processes, visually showing the classification proficiency of the model. The confusion matrix is shown in table format, with rows representing the true classes and columns indicating the predicted classes. The diagonal elements represent correct classifications for each class, while off-diagonal elements indicate incorrect classifications. By comparing the results between true and predicted classes, the accuracy of the ANN model in classifying various classes can be assessed. In Figure 4d and Figure S25 (Supporting information), the fabricated sensor demonstrates a high accuracy range from 91% to 99%. This result implies that the ANN model is highly effective at recognizing and classifying the different frequency elements of the fabricated sensor, thereby confirming the excellent capability in distinguishing different frequency elements.

### 2.5. Application of the Triboelectric Acoustic Sensor to Acoustic Human–Machine Interfaces (HMIs)

To realize the acoustic human–machine interface system, the microhair sensor is connected to a robotic hand, enabling it to

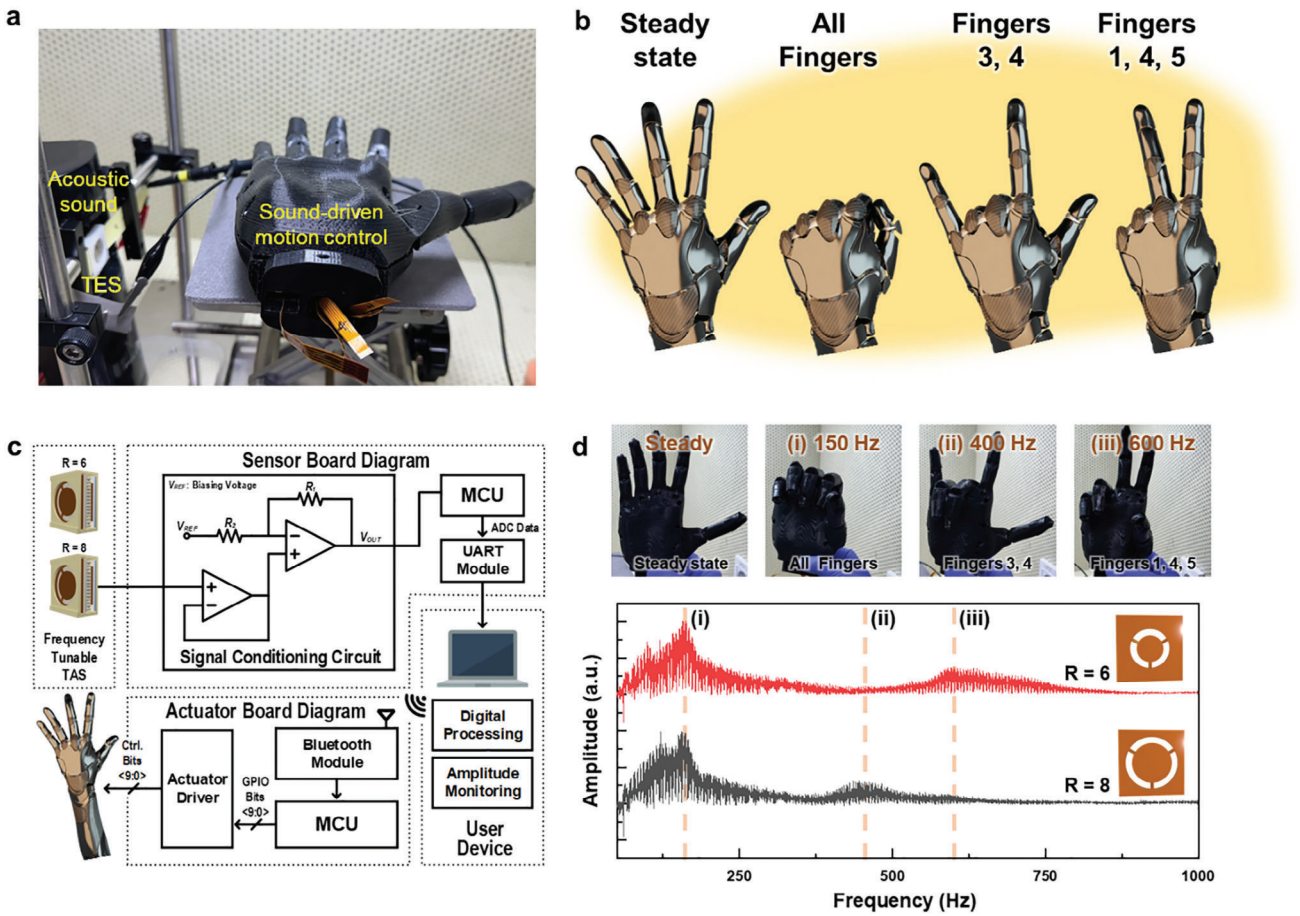


**Figure 5.** Application of the triboelectric acoustic sensor to acoustic human–machine interfaces (HMIs). a) Photograph of the demonstration setup of acoustic HMIs using the triboelectric sensor. b) Programmed robotic hand gestures at different frequencies. c) Circuit diagram showing connections between the fabricated sensors with two different diaphragms and the robotic hand. d) Plotted resonance frequencies and corresponding pictures of the programmed robotic hand gestures at different resonance frequencies.

respond to acoustic stimuli with programmed hand gestures. **Figure** 5a shows the fabricated sensor connected to the robotic hand. By modifying the diaphragm structure, the sensor can produce a reinforced output voltage at different resonance frequencies. This capability enables four different motion controls in the robotic hand, corresponding to different diaphragm structures and applied frequencies. Figure 5b illustrates the schematics of the programmed hand gestures (steady state, all fingers folded, fingers 3,4 folded, and fingers 1,4,5 folded) for the robotic hand in response to specific sound stimuli at each frequency region. For the control of the robotic hand, the entire system consists of two boards (modules) and a PC program (MATLAB) for signal processing and controlling the system (Figure 5c). The system includes a "Sensor" board, which reads the output from the fabricated sensor and sends signals to the control system, and an "Actuator" board, which interprets the control system's signals to operate the robotic hand. The sensor board reads signals amplified by a signal conditioning circuit and transmits them via UART as a wired output. The actuator board receives the data processed in MATLAB and controls five actuators to simulate various hand movements. A detailed description of the electric circuits can be found in Note S4 (Supporting Information). Video S1 (Supporting Information) demonstrates the implementation of the HMI electronic interface introduced above by mimicking a frequency-tunable TAS using a power supply. With our frequency tuning system, application in acoustic HMIs can be achieved (Figure 5d). We prepared two different diaphragms with two different resonance frequencies. Starting from the steady state, when the applied sound frequency reaches 150 Hz, i) all fingers of a robotic hand are folded. As we increase the applied frequency to the fabricated sensor, a diaphragm with an 8 mm radius shows a resonance frequency peak ≈400 Hz. Responding to the resonance frequency peak, ii) fingers 3,4 are folded. After changing the diaphragm to a 6 mm radius, a resonance frequency peak is observed ≈600 Hz, resulting in iii) fingers 1,4,5 being folded as a response to the tuned resonance peak. In Video S2 (Supporting Information), the control of the robotic hand with two different robotic hand gestures by tuning the resonance frequency by changing the diaphragm is demonstrated.

## 3. Conclusion

In this study, we have successfully developed a highly sensitive, self-powered, and frequency-tunable triboelectric acoustic

sensor inspired by the structure and function of the human cochlea. By mimicking the tapered hair cells found in the organ of Corti, we engineered a unique microhair structure using a ferroelectric PVDF-HFP/BTNP composite. This biomimetic design significantly enhanced the sensitivity to acoustic stimuli, with the tapered microhair structure demonstrating a 16-fold increase in output voltage compared to the planar structure. Furthermore, we addressed the limitation of fixed resonance frequency in conventional triboelectric acoustic sensors by introducing a microscale patterned diaphragm. Drawing inspiration from the structural variations of the basilar membrane, we designed a mass-beam diaphragm with kirigami cut patterns, enabling precise tuning of the sensor's resonance frequency through modification of the radius of the mass-beam diaphragm and the length of the kirigami pattern, covering a range from 400 to 900 Hz. The triboelectric sensor with the tapered microhair and the kirigami-patterned mass-beam structures exhibited a sensitivity of 860 mV $Pa^{-1}$, which is 31 times higher than that (28 mV $Pa^{-1}$) of the sensor without these biomimetic structures. This feature enables the sensor to differentiate human voices with different frequencies, highlighting its potential for speech recognition applications. Moreover, the reliability of our sensor was verified using an artificial neural network (ANN) model, which exhibited high accuracy in classifying the different frequency elements of the fabricated sensor. To showcase the practical application of our sensor in acoustic human–machine interfaces, we integrated it with a robotic hand capable of responding to acoustic stimuli with programmed hand gestures. By modifying the diaphragm structure, we achieved four different motion controls in the robotic hand, corresponding to specific sound stimuli at each frequency region. This demonstration underscores the potential of our frequency-tunable triboelectric acoustic sensor in advancing the field of intuitive and user-friendly human–machine interfaces.

## 4. Experimental Section

*Fabrication of Tapered Microhair Pattern on Si Wafer*: Negative photoresist (AZ nLOF 5510) is spin-coated on a Si wafer. A photomask with a 4 µm diameter, and 4 µm spacing hole pattern was used for the UV irradiation process of photolithography. The negatively hole-patterned Si wafer underwent Cr deposition by the evaporation method. The photoresist was subsequently removed with a piranha solution. To create a microhair pattern, a deep reactive ion etching (DRIE) process was performed using $SF_6$ and $C_4F_8$ gases for etching and passivation processes (process step – $SF_6$ 500 sccm at 40 W for 2 s and at 10 W for 7 s, $C_4F_8$ 300 sccm at 10 W for 6 s). Etching time differs for the fabrication of different aspect ratios (A.R. 3–7 min, A.R. 4–10 min, A.R. 5–11 min 30 s). After the microhair patterns were made, the top Cr layer was etched by Cr etchant to create a tapered pattern. The pattern surface was cleaned with piranha solution ($H_2SO_4$ added with $H_2O_2$ at 3:1 volume ratio), and the surface $SiO_2$ was etched by buffered oxide etchant (Transene Company, Inc.) for isotropic etching of Si. After that, isotropic etching was performed with RSE-100 solution (Transene Company, Inc.), which contains hydrofluoric acid, nitric acid, and acetic acid. After immersing in RSE-100 for 10–15 s, the tapered microhair pattern (1.75 cm x 1.75 cm) was achieved.

*Fabrication of Bottom Layer–Replica Molding Process*: The fabricated tapered microhair Si pattern was SAM-coated with FOTS solution (Sigma-Aldrich). $O_2$ plasma treatment (5 W, 25 sccm, Tergeo) was applied to the fabricated pattern for 5 min and 200 µl of FOTS solution was placed inside of a vacuum oven. The vacuum was turned on for 30 min to create a FOTS atmosphere inside the oven, which was then heated to 85 °C. After 30 min, the Si wafer was loaded for 90 min. After the SAM coating process, 8 g of PDMS (10:1, SYLGARD 184, DOW CORNING) was poured into a petri dish containing the microhair pattern. After 5 min of vacuum treatment to remove pores, the PDMS was heated at 80 °C for 3 h. The PDMS mold was gently peeled off.

*Fabrication of Ferroelectric PVDF-HFP/BTNP Films*: The 1 g of PVDF-HFP (427187, Sigma-Aldrich) was mixed with 7 g of DMF (DAEJUNG), and 7 wt.% of BTNP (US Research Nanomaterials Inc.) relative to the PVDF-HFP amount. The mixture was stirred for 5 h and 300 µL of the solution was cast on the fabricated PDMS mold. The cast mold underwent vacuum treatment for 5 min, and the PDMS mold was gently tapped to remove pores inside the mold. The casted solution was annealed at 140 °C for 2 h. The fabricated film was gently peeled off from the mold. A 3 nm Cr layer and a 100 nm Au layer were evaporated on the back of the fabricated film by a thermal evaporator (GV Tech). A Ni-Cu electrode was connected to the Au-evaporated film using Ag paste (ELCOAT, SANS).

*Fabrication of Top Layer*: A parylene layer was coated on a 2 cm × 2 cm glass substrate covered with a MICRO-90 sacrificial layer (surfactant). After coating the parylene-C to a thickness of ≈2 µm, a 100 nm thick Al layer was sputtered on the surface of the parylene-C film by RF sputtering. The side of the parylene-C-covered glass was cut with a razor blade, and a Ni-Cu electrode was connected to the Al-sputtered side of the parylene-C using Ag paste (ELCOAT, CANS). A 15 µm-thick double-sided tape was cut into a 2 cm × 2 cm outer square and a 1.25 cm × 1.25 cm inner square. The hollow square-shaped double-sided tape was attached to the surface of the parylene-C. A 90 nm thick double-sided PI tape was cut into 3 mm × 20 mm and attached at each end of the hollow-shaped double-sided tape. The MICRO-90 sacrificial layer was eliminated by immersing the glass in DI water.

*Fabrication of Diaphragm*: A 125 µm thick Kapton film was laser-printed into a uniquely patterned mass-beam structure using a laser cutter. The fabricated diaphragm had dimensions of 20 mm × 25 mm with three different 2.4 mm × 1 mm sized beams. A 90 nm thick double-sided PI tape was cut into 3 mm × 20 mm strips and attached at each end.

*Kirigami Structure*: One cycle of the kirigami pattern was 0.6 mm, composed of 3 cut patterns and 2 cut patterns. The 3 cut patterns had two short parts and one long part (1:3 ratio), while the 2 cut patterns had two long parts. The length of the kirigami structure indicated in Figure S20 (Supporting information) was the long part of the kirigami cut patterns. The cycle of the kirigami pattern was fixed at 3. As the diaphragm radius decreased from 8 to 3 mm, the long part of the kirigami cut patterns decreased from 0.9 to 0.4 mm.

*Measurement of Polarization-Electric Field Hysteresis Loop*: The PVDF-HFP/BTNP solution was prepared under the conditions described in the fabrication method. A 3 nm Cr layer and 100 nm Au layer were evaporated onto glass. Then, the PVDF-HFP/BTNP solution was spin-coated twice at 1000 rpm for 60 s. Finally, the same condition of Au/Cr was evaporated onto the fabricated film. The obtained PVDF-HFP/BTNP film was ≈1 µm thick. The Polarization-Electric filed hysteresis loop was measured by Precision LC II ferroelectric tester (Radiant Technologies Inc.).

*Measurement of Microphone Performance*: A frequency oscillator was connected to the incident speaker. The top layer, bottom layer, and diaphragm were attached to each other. The attached sensor and the incident speaker were placed inside an anechoic chamber. The fabricated microphone was fixed to a clamp with a width of 7.5 cm and a height of 10.5 cm in front of the incident speaker, maintaining a distance of 0.5 cm between the speaker and the microphone. A sound level meter was placed at the same distance (0.5 cm) to calibrate the decibel signals from the incident speaker. The $dB_A$ value was converted into $dB_{SPL}$ and calculated to pressure values based on auditory threshold ($2 \times 10^{-5}$ Pa). By using the frequency oscillator connected to the incident speaker, a frequency sweeping test (frequency range 50–10 000 Hz) was performed, and the output voltage test at different sound pressures was achieved by changing the applied $V_{rms}$ of the frequency oscillator. The fabricated microphone was connected to an oscilloscope to read the self-powered signals generated by triboelectrification between Al layer and PVDF-HFP/BTNP tapered microhair film.

*Verification of Sensor Reliability by Artificial Neural Network (ANN) System*: The ANN network used for sensor verification is composed of three different layers: an input layer, a hidden layer, and an output layer. The input layer for loading 5000 different pre-processed input data consisted of 1024 nodes. Two different hidden layers contain 512 and 64 nodes each. The output layer is composed of four different nodes, allowing the machine-learned data to predict one sensor with one specific diaphragm that matches the sweeping data and diaphragm information. Nonlinearity was introduced to the neural network of the input layer and hidden layers, which is crucial for learning the complicated pattern within the given data during the learning processes. In addition, the rectified linear unit (ReLU) activation function was used for the approximation and handling of the nonlinear relations within the data by the ANN model. For the output layer, the sigmoid activation function was used to take advantage of its direct connection between the artificial neural network output and the proper class's probability within the binary classification process. Through the sigmoid activation function, the machine-learning data was acquired at the output layer.

*Characterization*: The structures and morphologies of the hierarchical ferroelectric structure were characterized using field-emission SEM (SU-8220, Hitachi, Japan). The self-powered acoustic signals were read by an oscilloscope (Tektronix, DPO2024B), and an incident speaker (PILLAR, CS-5100) was connected to a frequency oscillator (SG-3428B, Sigma eltech). A sound level meter (TENMARS, TM-102) was used as a calibrated microphone for THD evaluation. Photolithography was performed using a mask aligner (Suss Microtec, MA/BA 6–8). The relative permittivity was measured by an impedance analyzer (IM3570, HIOKI). ANN models were realized using Python 3.11.4 with related packages such as NumPy 1.24.3, pandas 1.5.3, and Keras 2.14.0. This model was run on a computer with a 2.10 GHz 12th Gen Intel(R) Core(TM) i7-12700 CPU, 32GB RAM, and an Inter(R) UHD Graphics 770 GPU.

*Finite Element Calculation*: Theoretical simulations of stress distribution, electrical potential during triboelectrification, and resonance frequency analysis were performed using COMSOL 5.4 Multiphysics.

## Supporting Information

Supporting Information is available from the Wiley Online Library or from the author.

## Acknowledgements

D.K., H.L., and M.S. contributed equally to this work. This work was supported by the National Research Foundation (NRF) of Korea (2021R1A2C3009222, 2022M3H4A1A02076825).

## Conflict of Interest

The authors declare no conflict of interest.

## Data Availability Statement

The data that support the findings of this study are available from the corresponding author upon reasonable request.

## Keywords

acoustic sensor, bio-inspired device, ferroelectric composite, human cochlea, triboelectric device

Received: May 15, 2024
Revised: September 15, 2024
Published online:

[1] J. Park, Y. Lee, S. Cho, A. Choe, J. Yeom, Y. G. Ro, J. Kim, D. Kang, S. Lee, H. Ko, *Chem. Rev.* **2024**, *124*, 1464.
[2] J.-H. Lee, K. H. Cho, K. Cho, *Adv. Mater.* **2023**, *35*, 2209673.
[3] Y. H. Jung, S. K. Hong, H. S. Wang, J. H. Han, T. X. Pham, H. Park, J. Kim, S. Kang, C. D. Yoo, K. J. Lee, *Adv. Mater.* **2020**, *32*, 1904020.
[4] Z. Lin, S. Duan, M. Liu, C. Dang, S. Qian, L. Zhang, H. Wang, W. Yan, M. Zhu, *Adv. Mater.* **2024**, *36*, 2306880.
[5] Y. Jiang, Y. Zhang, C. Ning, Q. Ji, X. Peng, K. Dong, Z. L. Wang, *Small.* **2022**, *18*, 2106960.
[6] K. Ma, H. Chen, Z. Wu, X. Hao, G. Yan, W. Li, L. Shao, G. Meng, W. Zhang, *Sci. Adv.* **2022**, *8*, eadc9230.
[7] Z. Lin, G. Zhang, X. Xiao, C. Au, Y. Zhou, C. Sun, Z. Zhou, R. Yan, E. Fan, S. Si, L. Weng, S. Mathur, J. Yang, J. Chen, *Adv. Funct. Mater.* **2022**, *32*, 2109430.
[8] J. Park, D. Kang, H. Chae, S. K. Ghosh, C. Jeong, Y. Park, S. Cho, Y. Lee, J. Kim, Y. Ko, J. J. Kim, H. Ko, *Sci. Adv.* **2022**, *8*, eabj9220.
[9] Y. Liu, J. J. S. Norton, R. Qazi, Z. Zou, K. R. Ammann, H. Liu, L. Yan, P. L. Tran, K.-I. Jang, J. W. Lee, D. Zhang, K. A. Kilian, S. H. Jung, T. Bretl, J. Xiao, M. J. Slepian, Y. Huang, J.-W. Jeong, J. A. Rogers, *Sci. Adv.* **2016**, *2*, e1601185.
[10] Y. H. Jung, T. X. Pham, D. Issa, H. S. Wang, J. H. Lee, M. Chung, B.-Y. Lee, G. Kim, C. D. Yoo, K. J. Lee, *Nano Energy.* **2022**, *101*, 107610.
[11] Y. Wang, L. Wang, T. Yang, X. Li, X. Zang, M. Zhu, K. Wang, D. Wu, H. Zhu, *Adv. Funct. Mater.* **2014**, *24*, 4666.
[12] S. Lee, J. Kim, I. Yun, G. Y. Bae, D. Kim, S. Park, I.-M. Yi, W. Moon, Y. Chung, K. Cho, *Nat. Commun.* **2019**, *10*, 2468.
[13] Y. Ma, Y. Yue, H. Zhang, F. Cheng, W. Zhao, J. Rao, S. Luo, J. Wang, X. Jiang, Z. Liu, N. Liu, Y. Gao, *ACS Nano.* **2018**, *12*, 3209.
[14] K. Kim, M. Ha, B. Choi, S. H. Joo, H. S. Kang, J. H. Park, B. Gu, C. Park, C. Park, J. Kim, S. K. Kwak, H. Ko, J. Jin, S. J. Kang, *Nano Energy.* **2018**, *48*, 275.
[15] H. Ding, Z. Zeng, Z. Wang, X. Li, T. Yildirim, Q. Xie, H. Zhang, S. Wageh, A. A. Al-Ghamdi, X. Zhang, B. Wen, *Adv. Intell. Syst.* **2022**, *4*, 2200140.
[16] G.-Y. Gou, X.-S. Li, J.-M. Jian, H. Tian, F. Wu, J. Ren, X.-S. Geng, J.-D. Xu, Y.-C. Qiao, Z.-Y. Yan, G. Dun, C. W. Ahn, Y. Yang, T. L. Ren, *Sci. Adv.* **2022**, *8*, eabn2156.
[17] S. A. U. Hasan, Y. Jung, S. Kim, C.-L. Jung, S. Oh, J. Kim, H. Lim, *Sensors.* **2016**, *16*, 93.
[18] X. Chen, Q. Zeng, J. Shao, S. Li, X. Li, H. Tian, G. Liu, B. Nie, Y. Luo, *ACS Appl. Mater. Interfaces.* **2021**, *13*, 34637.
[19] H. Guo, X. Pu, J. Chen, Y. Meng, M.-H. Yeh, G. Liu, Q. Tang, B. Chen, D. Liu, S. Qi, C. Wu, C. Hu, J. Wang, Z. L. Wang, *Sci. Robot.* **2018**, *3*, eaat2516.
[20] S. Lee, J.-W. Park, *Nano Energy.* **2022**, *101*, 107546.
[21] S. Lee, J. Kim, H. Roh, W. Kim, S. Chung, W. Moon, K. Cho, *Adv. Mater.* **2022**, *34*, 2109545.
[22] S. Lee, H. Roh, J. Kim, S. Chung, D. Seo, W. Moon, K. Cho, *Adv. Mater.* **2022**, *34*, 2205537.
[23] Y. Zhao, S. Gao, X. Zhang, W. Huo, H. Xu, C. Chen, J. Li, K. Xu, X. Huang, *Adv. Funct. Mater.* **2020**, *30*, 2001553.
[24] X. Chen, H. Guo, H. Wu, H. Chen, Y. Song, Z. Su, H. Zhang, *Nano Energy.* **2018**, *49*, 51.
[25] C. Zheng, L. Xu, X. Fan, J. Yang, J. Fan, X. Huang, *J. Acoust. Soc. Am.* **2022**, *151*, 2814.
[26] S. Park, X. Guan, Y. Kim, F. X. Creighton, E. Wei, I. Kymissis, H. H. Nakajima, E. S. Olson, *Trends Hear.* **2018**, *22*, 2331216518774450.
[27] B. Duan, K. Wu, X. Chen, J. Ni, X. Ma, W. Meng, K. Lam, P. Yu, *Adv. Electron. Mater.* **2023**, *9*, 2300348.
[28] A. Kumar, M. Prasad, V. Janyani, R. Yadav, *Microsyst. Technol.* **2019**, *25*, 4517.
[29] C. Lang, J. Fang, H. Shao, X. Ding, T. Lin, *Nat. Commun.* **2016**, *7*, 11108.

[30] W. Yan, G. Noel, G. Loke, E. Meiklejohn, T. Khudiyev, J. Marion, G. Rui, J. Lin, J. Cherston, A. Sahasrabudhe, J. Wilbert, I. Wicaksono, R. W. Hoyt, A. Missakian, L. Zhu, C. Ma, J. Joannopoulos, Y. Fink, *Nature.* **2022**, *603*, 616.
[31] H. S. Lee, J. Chung, G.-T. Hwang, C. K. Jeong, Y. Jung, J.-H. Kwak, H. Kang, M. Byun, W. D. Kim, S. Hur, S.-H. Oh, K. J. Lee, *Adv. Funct. Mater.* **2014**, *24*, 6914.
[32] Y. H. Jung, J. An, D. Y. Hyeon, H. S. Wang, I. Kim, C. K. Jeong, K.-I. Park, P. S. Lee, K. J. Lee, *Adv. Funct. Mater.* **2024**, *34*, 2309316.
[33] H. S. Wang, S. K. Hong, J. H. Han, Y. H. Jung, H. K. Jeong, T. H. Im, C. K. Jeong, B.-Y. Lee, G. Kim, C. D. Yoo, K. J. Lee, *Sci. Adv.* **2021**, *7*, eabe5683.
[34] X. Fan, J. Chen, J. Yang, P. Bai, Z. Li, Z. L. Wang, *ACS Nano.* **2015**, *9*, 4236.
[35] R.-H. Horng, K.-F. Chen, Y.-C. Tsai, C.-Y. Suen, C.-C. Chang, *J. Micromech. Microeng.* **2010**, *20*, 065004.
[36] A. Yu, M. Song, Y. Zhang, Y. Zhang, L. Chen, J. Zhai, Z. L. Wang, *Nano Res.* **2015**, *8*, 765.
[37] Y. Liu, Y. Zhu, J. Liu, Y. Zhang, J. Liu, J. Zhai, *Nanoscale Res. Lett.* **2018**, *13*, 191.
[38] H. M. A. Hamid, Z. Celik-Butler, presented at *2019 IEEE Sensors Applications Symp. (SAS)*, March, **2019**.
[39] H. Zhang, L. Quan, J. Chen, C. Xu, C. Zhang, S. Dong, C. Lü, J. Luo, *Nano Energy.* **2019**, *56*, 700.
[40] S. Milici, J. Lorenzo, A. Lázaro, R. Villarino, D. Girbau, *IEEE Sens. J.* **2017**, *17*, 1285.
[41] R. Xu, F. Luo, Z. Zhu, M. Li, B. Chen, *ACS Appl. Electron. Mater.* **2022**, *4*, 4051.
[42] H. Yu, H. Guo, J. Wang, T. Zhao, W. Zou, P. Zhou, Z. Xu, Y. Zhang, J. Zheng, Y. Zhong, X. Wang, L. Liu, *Adv. Sci.* **2024**, *11*, 2305883.
[43] S. E. Hayber, T. E. Tabaru, O. G. Saracoglu, *Opt. Commun.* **2019**, *430*, 14.
[44] T. C. Shyu, P. F. Damasceno, P. M. Dodd, A. Lamoureux, L. Xu, M. Shlian, M. Shtein, S. C. Glotzer, N. A. Kotov, *Nat. Mater.* **2015**, *14*, 785.
[45] T. A. Hamill, L. L. Price, *The Hearing Sciences*, Plural Publishing, San Diego, CA **2017**.
[46] B. C. J. Moore, *Hearing*, Academic, San Diego; London **1995**.
[47] J. H. Han, J.-H. Kwak, D. J. Joe, S. K. Hong, H. S. Wang, J. H. Park, S. Hur, K. J. Lee, *Nano Energy.* **2018**, *53*, 198.
[48] Y. Park, Y.-E. Shin, J. Park, Y. Lee, M. P. Kim, Y.-R. Kim, S. Na, S. K. Ghosh, H. Ko, *ACS Nano.* **2020**, *14*, 7101.
[49] Y. Zhou, J. Tan, J. Wu, Q. Zhang, J. Andre, C. Xi, Z. Chen, M. E. Meyerhoff, *Acta Biomater.* **2019**, *90*, 112.
[50] A. Poudel, M. Fernandez-Yague, S. A. M. Tofail, M. J. P. Biggs, *Front. Chem.* **2019**, *7*, 364.
[51] R. Peng, B. Zhang, G. Dong, Y. Wang, G. Yang, J. Zhang, B. Peng, Y. Zhao, M. Liu, *Adv. Funct. Mater.* **2024**, *34*, 2316519.
[52] P. Kim, S. C. Jones, P. J. Hotchkiss, J. N. Haddock, B. Kippelen, S. R. Marder, J. W. Perry, *Adv. Mater.* **2007**, *19*, 1001.
[53] S. Chun, C. Pang, S. B. Cho, *Adv. Mater.* **2020**, *32*, 1905539.
[54] J. Jeong, S. Jeon, X. Ma, Y. W. Kwon, D.-M. Shin, S. W. Hong, *Adv. Mater.* **2021**, *33*, 2102530.
[55] V.-T. Bui, Q. Zhou, J.-N. Kim, J.-H. Oh, H.-S. Choi, S.-W. Kim, I.-K. Oh, *Adv. Funct. Mater.* **2019**, *29*, 1901638.
[56] H. Taniyama, E. Iwase, *Micromachines.* **2019**, *10*, 395.
[57] A. T. Haque, D. Hwang, M. D. Bartlett, *Adv. Mater. Technol.* **2022**, *7*, 2101241.
[58] S. Gandla, J. Song, J. Shin, S. Baek, M. Lee, D. Khan, K.-Y. Lee, J. H. Kim, S. Kim, *ACS Appl. Mater. Interfaces.* **2021**, *13*, 54162.
[59] Y. Qi, Y. Kuang, Y. Liu, G. Liu, J. Zeng, J. Zhao, L. Wang, M. Zhu, C. Zhang, *Appl. Energy.* **2022**, *327*, 120092.